

Measurement report: Crustal materials play an increasing role in elevating particle pH: Insights from 12-year records in a typical inland city of China.

Hongyu Zhang^{1,2}, Shenbo Wang^{2,3*}, Zhangsen Dong^{1,2*}, Xiao Li^{2,3}, Ruiqin Zhang^{2,3}

¹ Collage of Chemistry, Zhengzhou University, Zhengzhou, 450000, China

² Research Institute of Environmental Sciences, Zhengzhou University, Zhengzhou 450000, China

³ School of Ecology and Environment, Zhengzhou University, Zhengzhou, 450000, China

* Corresponding authors: Shenbo Wang and Zhangsen Dong

E-mail address: shbwang@zzu.edu.cn and dzszzu1990@163.com

14 **Abstract**

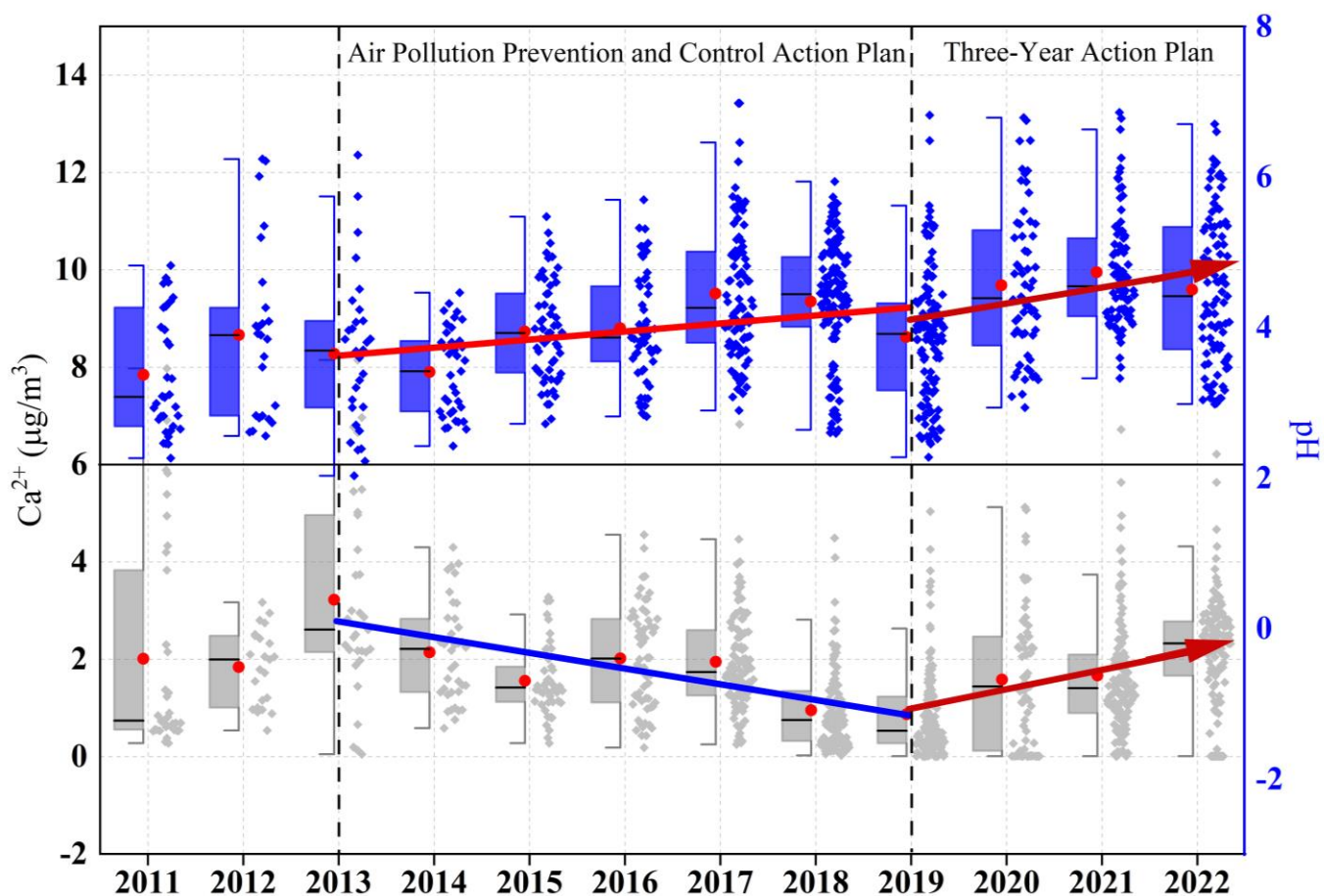
15 Particle acidity serves as a key determinant in atmospheric chemical processes. Emerging concerns
16 regarding aerosol acidity trends have been highlighted amid China's sustained initiatives to mitigate
17 emissions of both acidic and alkaline precursors, especially in North China, which is significantly
18 affected by dust aerosol. 12-year observational data in Zhengzhou reveal that the annual average PM_{2.5}
19 concentration decreased from $162 \pm 81 \text{ } \mu\text{g}/\text{m}^3$ in 2011 to $60 \pm 41 \text{ } \mu\text{g}/\text{m}^3$ in 2022, with the largest
20 reduction in sulfate (73%). Correspondingly, the annual particle pH increased by 0.10 units from 2011
21 to 2019. In addition, the elevated particle pH in 2015 and 2018 was notably influenced by the increase
22 in TNH_x (NH₃ + NH₄⁺). Note that the crustal material concentrations and their proportions increased
23 significantly during 2019–2022, which might be responsible for the resuspension of surrounding soil
24 dust. Even though the TNH_x concentration was decreasing, the annual average growth rate of pH
25 values increased to 0.21 units from 2019 to 2022. This phenomenon is not unique to Zhengzhou, as
26 major cities in the North China Plain have also experienced a pronounced upward trend in coarse
27 particles after 2019. Therefore, the long-term evolution of particle acidity in North China will require
28 comprehensive consideration of synergistic effects involving acidic precursors, ammonia, and crustal
29 materials.

30 **Keywords:** Dust, aerosol acidity, sources, North China Plain, control measurement

31

32 **Synopsis:** The future ammonia reduction policies in North China may not lead to a rapid increase in
33 particle acidity in the presence of crustal materials., which further elevated the particle pH after 2019.

34 **Graphical abstract:**



38 **Highlights:**

- 39 • Crustal material concentrations and their proportions increased significantly during 2019–2022;
- 40 • The resuspension of surrounding soil dust may determine the rebound of crustal material concentrations;
- 42 • Rebound in crustal material further elevated the particle pH.

44 **1 Introduction**

45 Particle acidity is a critical parameter that affects atmospheric chemistry, such as the gas-particle
46 partitioning of semi-volatile and volatile species (Surratt et al., 2010; Guo et al., 2016), the solubility
47 of metals (Tao and Murphy, 2019), acid-catalyzed reactions (Rengarajan et al., 2011), and acid
48 deposition (Mao et al., 2009), thereby determining aerosol concentration and chemical composition,
49 as well as impacting human health, ecosystems, and climate (Li et al., 2017; Pye et al., 2020; Su et al.,
50 2020; Nenes et al., 2021). Generally, the global fine particulate matter (PM_{2.5}, aerodynamic diameter
51 ≤ 2.5 μm) exhibits a bimodal pH distribution ranging from 1–3 (e.g., in the United States and Europe)
52 (Guo et al., 2015; Battaglia et al., 2017; Masiol et al., 2020; Zhang et al., 2021) and 4–5 (e.g., in East
53 Asia) (Kim et al., 2022; Sharma et al., 2022). The atmosphere rich in gaseous ammonia (NH₃) and
54 crustal material (CM) shows significant pH buffering effects (Wang et al., 2020; Zheng et al., 2020;
55 Karydis et al., 2021), which is a dominant factor that drives the high particle pH in East Asia (Karydis
56 et al., 2021; Zhang et al., 2021; Kim et al., 2022; Sharma et al., 2022).

57 In recent years, the changing trends in particle pH have become a research focus, especially in
58 China, in response to air pollution control policies, i.e. Air Pollution Prevention and Control Action
59 Plan (2013–2018) and Three-Year Action Plan (2018–2020). The annual average PM_{2.5} concentration
60 in Beijing dropped by 64% from 89.5 $\mu\text{g}/\text{m}^3$ in 2013 to 32 $\mu\text{g}/\text{m}^3$ in 2023 (MEP, 2023), with a clear
61 downward trend of sulfate concentration, and nitrate surpassing sulfate as the primary component
62 (Zhai et al., 2019; Zhou et al., 2019; Li et al., 2023). The atmospheric behavior of ammonium, governed
63 by gas-particle partitioning processes involving ammonia (NH₃) as the predominant alkaline gas,

64 demonstrates notable stability in concentration levels, with observational records showing less than 5%
65 interannual variation in NH_3 column densities over North China during 2015–2019 (Dong et al., 2023).
66 Under such conditions, the dominant inorganic aerosol component transitions from ammonium sulfate
67 to ammonium nitrate. This compositional shift enhances atmospheric particulate hygroscopicity due
68 to ammonium nitrate’s superior water uptake capability, ultimately elevating particle pH levels through
69 aqueous-phase dilution mechanisms (Wexler and Seinfeld, 1991; Pinder et al., 2007, 2008; Heald et
70 al., 2012; Weber et al., 2016). For instance, a significant increase in the nitrate-to-sulfate molar ratio
71 from 2014–2017 in Beijing resulted in the particle pH increasing from 4.4 to 5.4 (Xie et al., 2020).
72 Moreover, increased NH_3 concentrations raised particle pH by 0.3–0.4 units from 2014/2015 to
73 2018/2019 in Beijing (Song et al., 2019). Over Europe and North America, the pH has increased
74 strongly from about 2.8 and 2.2 during the 1970s to 3.9 and 3.3 in 2020 respectively, especially during
75 the 1990s, with significantly increasing NH_3 emission (Karydis et al., 2021). On the contrary, modeling
76 results indicate a continuous decline in pH in East Asia from 1970 to 2020 due to sharp increases in
77 SO_2 and NO_x emissions (Karydis et al., 2021). In addition, the $\text{PM}_{2.5}$ pH showed a slight decrease of
78 0.13 from 2018 to 2022 summer in Beijing due to the change in total nitrate ($\text{NO}_3^- + \text{HNO}_3$) (Li et al.,
79 2023). Moreover, Zhou et al. (2022) found a decreasing pH trend from 2011 to 2019 in eastern China,
80 primarily influenced by temperature, followed by sulfate and non-volatile cations. Similarly, Nah et al.
81 (2023) observed a decreasing pH trend from 2011 to 2020 in Hong Kong, attributing it to temperature
82 and sulfate levels. Thus, concerns have been raised about the potential increase in the acidity of aerosol
83 and precipitation due to China’s ongoing efforts to reduce ammonia emissions, which pose severe
84 health risks and acid deposition (Liu et al., 2019; Shi et al., 2019).

85 In addition to NH_3 , CM is another key alkaline substance, that buffers particle pH. Ca^{2+} can form
86 insoluble CaSO_4 with sulfate, reducing sulfate concentration in the aqueous phase of aerosol, and thus
87 lowering H^+ and aerosol liquid water content (ALWC) concentrations and enhancing particle pH (Ding
88 et al., 2019; Karydis et al., 2021). Moreover, non-volatile cations can lower the molar ratio of ammonia
89 to sulfate, leading to an increase in particle pH (Zheng et al., 2022). Karydis et al. (2021) framework
90 demonstrated that CM played a critical buffering role in sustaining aerosol pH around 7 across the
91 Middle East arid regions. The model sensitivity tests revealed that under hypothetical dust-free
92 conditions ($\text{CM} = 0$), aerosol acidity would escalate to $\text{pH} \sim 4$ due to $\text{NH}_4^+/\text{SO}_4^{2-}$ domination. Wang et
93 al. (2022) reported that non-volatile cations accounted for approximately 8–17% of hourly aerosol pH
94 variation. Li et al. (2023) indicated that the buffering effect of cations was the major reason for the
95 relatively small pH changes from 2018 to 2022 in Beijing, emphasizing that reducing coarse particle
96 emissions in the future could significantly decrease particle pH. In addition, there was a rising trend in
97 the contribution of CM to particle pH in Tianjin, China (Shi et al., 2017). Therefore, it is evident that
98 CM has a significant impact on the variation of particle pH, especially in North China, which is
99 significantly affected by dust aerosol, but the trend of CM concentration and its long-term implication
100 is still lacking unfortunately.

101 Zhengzhou presents unique atmospheric chemistry that distinguishes it from other mega-cities in
102 North China. As the capital of China's foremost agricultural province (Henan Province, contributing
103 18% of national NH_3 emissions), Zhengzhou's $\text{PM}_{2.5}$ composition combined substantial crustal
104 material ($15 \pm 3\%$ in $\text{PM}_{2.5}$ vs. $<10\%$ in Beijing) with exceptional ammonia abundance (Huang et al.,
105 2012; Liu et al., 2018; Wang et al., 2018). This created distinct particle acidity characteristics,

maintaining pH 4.5–6.0 compared to lower pH levels (3.3–5.4) in other cities like Beijing (Ding et al., 2019; Zhang et al., 2021). However, two critical research gaps persist: (1) the long-term evolution of CM under control policies remains unquantified; (2) the role of CM on pH buffer capacity in NH_3 -enriched environments lacks systematic assessment.

To address these gaps, our study pioneers the first multi-decadal analysis (2011–2022) coupling $\text{PM}_{2.5}$ components with thermodynamic modeling through three key innovations: (1) revealing the long-term trends of CM, (2) analyzing the variations of CM sources, and (3) exploring pH trend and its relationship with CM. The resultant findings advance our understanding of urban aerosol acidity chemistry by underscoring the critical role of CM.

2 Experiment and method

2.1 Instruments and Measurements

Sampling was conducted on the fourth-floor platform at Zhengzhou University (34.75°N , 113.61°E) in Zhengzhou, China. The sampling site (Fig. S1), approximately 14 m above the ground, is primarily surrounded by residential areas with well-developed transportation networks and no significant industrial sources. There are two highways located 3 km to the south and 7 km to the east. Additionally, a coal-fired power plant located 6 km to the east was shut down in 2020, and a gas-fired power plant is situated 3 km to the south.

Samples were collected using a high-volume sampler (TE-6070D, Tisch, USA) and air particulate samplers (TH-16A, Tianhong, China) from April 2011 to December 2022. Two quartz filters and two

125 Teflon filters were used daily from 10:00 AM to 9:00 AM the next day, resulting in a total of 5848
126 samples. After excluding abnormal data due to instrument malfunctions, 4228 valid samples were
127 obtained. Detailed information on the samples is provided in Table S1. Organic carbon (OC) and
128 elemental carbon (EC) were analyzed using a carbon analyzer (Model 5L, Sunset Laboratory, USA).
129 Water-soluble inorganic ions (Cl^- , NO_3^- , SO_4^{2-} , Na^+ , NH_4^+ , K^+ , Mg^{2+} , and Ca^{2+}) were measured using
130 ion chromatography (ICS-90 and ICS-900 models, Dionex, USA) (Yu et al., 2017; Jiang et al., 2018).
131 Elements were analyzed using a wavelength dispersive X-ray fluorescence spectrometer (S8 TIGER,
132 Bruker, Germany) to determine concentrations of Fe, Na, Mg, Al, Si, Cl, K, Ca, V, Ni, Cu, Zn, Cr, Mn,
133 Co, Cd, Ga, As, Se, Sr, Sn, Sb, Ba, and Pb (Tremper et al., 2018). Meteorological conditions, including
134 temperature (T), relative humidity (RH), and wind speed (WS) were obtained using an automatic
135 weather station (Wang et al., 2019). Blank filters were also routinely analyzed with each batch of
136 samples to detect sample contamination and provide quality assurance on the elemental concentrations.
137 Detailed analytical methods and quality control are described in the supplement (Text S1). The method
138 detection limits and measurement uncertainties are summarized in Table S2. The quality assurance
139 protocol excluded temporally discrete dust storm and precipitation periods to prevent contamination
140 of the source analysis of CM and modeling particle pH, given that such events induce non-
141 representative extremes in both crustal element concentrations and pH values, coupled with elevated
142 PM measurement uncertainties. The annual mean $\text{PM}_{2.5}$ concentration data for cities in the North China
143 Plain were obtained from the China National Environmental Monitoring Center (CNEMC), available
144 at <https://www.cnemc.cn/>.

145 2.2 Data Analysis

146 2.2.1 Mass reconstruction

147 The calculation method for CM is as follows (Tian et al., 2016):

$$148 \quad [CM] = 1.89 \times [Al] + 2.14 \times [Si] + 1.4 \times [Ca] + 1.43 \times [Fe] + 1.94 [Ti] \quad (1)$$

149 where [Al], [Si], [Ca], [Fe] and [Ti] represent the concentrations of the respective elements ($\mu\text{g}/\text{m}^3$),

150 but Ti was not measured.

151 2.2.2 Thermodynamic model

152 The particle pH was calculated using the ISORROPIA-II mode (version 2.1,

153 <http://isorropia.eas.gatech.edu>). The input data (excluding $RH \leq 30\%$), including SO_4^{2-} , TNO_3 (HNO_3

154 $+$ NO_3^-), TNH_x ($\text{NH}_3 + \text{NH}_4^+$), Ca^{2+} , K^+ , Na^+ , Mg^{2+} , Cl^- , RH and T , with the temporal resolution aligned

155 with the sampling periods (from 10:00 AM to 9:00 AM the following day). Input data (excluding RH

156 $\leq 30\%$) included SO_4^{2-} , TNO_3 ($\text{HNO}_3 + \text{NO}_3^-$), TNH_x ($\text{NH}_3 + \text{NH}_4^+$), Ca^{2+} , K^+ , Na^+ , Mg^{2+} , Cl^- , RH and

157 T . The concentrations of hydrogen ions in air (H_{air}^+) and ALWC were calculated using the aerosol

158 equilibrium composition system $\text{Na}^+ - \text{K}^+ - \text{Ca}^{2+} - \text{Mg}^{2+} - \text{NH}_4^+ - \text{SO}_4^{2-} - \text{NO}_3^- - \text{Cl}^- - \text{H}_2\text{O}$ H_{air}^+ (Fountoukis

159 and Nenes, 2007). pH values were calculated using the following formula:

$$160 \quad \text{pH} = -\log_{10} \text{H}_{\text{aq}}^+ \cong -\log_{10} \frac{1000 \text{H}_{\text{air}}^+}{\text{ALWC}_i + \text{ALWC}_o} \cong -\log_{10} \frac{1000 \text{H}_{\text{air}}^+}{\text{ALWC}_i} \quad (2)$$

$$161 \quad \text{ALWC}_o = \frac{m_{\text{org}} \rho_w}{\rho_w} \frac{\kappa_{\text{org}}}{\left(\frac{1}{RH} - 1 \right)} \quad (3)$$

162 where ALWC_i and ALWC_o refer to the ALWC for inorganic and organic components, respectively.

163 m_{org} denotes the mass of organic aerosol, ρ_w is the density of water (1.0 g/cm³), ρ_{org} is the density of
 164 organic material (1.4 g/cm³) (Guo et al., 2015), k_{org} is the hygroscopicity parameter for organic aerosol
 165 (0.087) (Chang et al., 2010; Li et al., 2016). The ISORROPIA-II model operated under metastable
 166 conditions in the forward mode. Due to the lack of measured data for gaseous HNO₃ and NH₃, TNO₃
 167 was represented solely by NO₃⁻. The concentration of NH₃ was simulated based on a linear regression
 168 equation proposed by Wei et al. (2023), who used the same data as this study from 2013 to 2020:

$$169 \quad \text{NH}_3 = 19.909 \times \text{RH} + 0.559 \times \text{T} - 0.35 \times \text{NH}_4^+ + 0.123 \times \text{NO}_3^- + 2.159 \times \text{Cl}^- - 0.224 \times \text{SO}_4^{2-} - 154.923 \quad (4)$$

170 where NO₃⁻, SO₄²⁻, NH₄⁺, and Cl⁻ correspond to their respective concentrations (μg/m³). To validate
 171 the applicability of Equation 4 for annual NH₃ estimation and pH simulation in Zhengzhou, this study
 172 utilized both observed NH₃ data (from a Thermo Scientific URG-9000D ambient ion monitor, USA)
 173 and calculated NH₃ values derived from Equation 4 at the same monitoring site throughout 2022,
 174 inputting them into the thermodynamic model for pH simulation. As shown in Figure S2, pH values
 175 calculated from observed and simulated NH₃ exhibit good agreement ($r = 0.97$, $P < 0.01$). Furthermore,
 176 NH₃ concentrations modeled by ISORROPIA demonstrate a significant correlation ($r = 0.95$, $P < 0.01$)
 177 with that simulated NH₃ by Equation 4. These results collectively demonstrate the reliability of the
 178 NH₃ estimation method in this study.

179 **2.2.3 HYSPLIT analysis**

180 Backward trajectories were calculated using the mixed-particle Lagrangian integrated trajectory
 181 method (HYSPLIT, [https:// www.ready.noaa.gov/HYSPLIT_traj.php](https://www.ready.noaa.gov/HYSPLIT_traj.php)). Meteorological input data were
 182 from the Global Data Assimilation System (GDAS) with 3D wind vectors, temperature, relative

183 humidity, geopotential height, surface pressure, and boundary layer diagnostics. 24-h backward
184 trajectories were simulated for air masses above 1000 m above ground level in Zhengzhou. While the
185 surface elevation of Zhengzhou is approximately 100 m above sea level (ASL), setting the height at
186 1000 m ASL takes into account the minimum altitude needed to traverse the average elevation of the
187 Taihang Mountains (ranging from 1000 to 1500 m ASL). This ensures that the simulated trajectory
188 paths over this topographical barrier are physically realistic.

189 The Angle Distance algorithm was used to cluster air mass trajectories, enabling the identification
190 of dominant air mass directions and potential pollution sources affecting the study site during different
191 periods. The optimal number of clusters was determined by evaluating the spatial variance (SPVAR)
192 of each trajectory from the cluster mean and the total spatial variance (TSV). The final classification
193 was selected just before the second rapid increase in TSV. The underlying principle is that TSV initially
194 rises sharply during clustering, then increases gradually; however, once the number of clusters reaches
195 a certain threshold, TSV surges again, indicating that the merged clusters are highly dissimilar, marking
196 the end of the classification process. The classification results correspond to the different air mass
197 categories before this final merging step. The mean trajectories of these clusters represent the primary
198 airflow patterns at the target site during the analysis period (Wang et al., 2009). Subsequently,
199 trajectories from two periods, 2013–2018 and 2019–2022, were clustered separately to analyze the
200 variations between the two policy implementation periods.

201 **3 Results and discussion**

202 **3.1 Temporal variations in chemical components**

203 Over the past twelve years, the Chinese government implemented the Air Pollution Prevention
204 and Control Action Plans (2013–2018) and the Three-Year Action Plan (2018–2020). The Air Pollution
205 Prevention and Control Action Plan focused on reducing PM_{2.5} concentrations in key regions and
206 aiming to cut PM_{2.5} levels by 10–25% in priority areas over five years. To achieve these goals, it
207 adopted several measures. In terms of industrial restructuring, it mandated the elimination of a large
208 amount of outdated production capacity in industries such as iron/steel and cement to optimize the
209 industrial structure and reduce high-pollution production. For emission standards, it set strict
210 requirements for multiple industrial sectors, especially coal-fired power plants, and gradually
211 introduced ultra-low emission requirements to control pollutants like SO₂, NO_x, and PM. Regarding
212 energy transition, it promoted a shift from coal to cleaner energy sources, including capping coal
213 consumption in certain regions and restricting the construction of small-scale coal-fired boilers.
214 Subsequently, the Three-Year Action Plan was carried out to continue improving air quality with a
215 broader scope of regions under control, further reducing pollutant emissions and enhancing the overall
216 air quality index. The measures included enhanced transportation controls, such as introducing stricter
217 vehicle emission standards (like National VI standards for vehicles) and establishing diesel truck
218 exclusion zones in many cities to reduce emissions from the transportation sector. It also adopted
219 precision governance through grid-based environmental supervision, dividing areas into small grids
220 for more accurate and efficient monitoring of pollution sources. Additionally, it strengthened the legal

221 and institutional framework by revising relevant laws, such as the Air Pollution Prevention and Control
222 Law, to strengthen legal penalties for environmental violations and implementing an environmental
223 tax system to encourage enterprises to reduce emissions.

224 The long-term trends in PM_{2.5} concentrations and its chemical components in Zhengzhou from
225 2011 to 2022 are depicted in Fig. 1, with annual average concentrations listed in Table 1.
226 Correspondingly, the annual average concentration of PM_{2.5} in Zhengzhou decreased from 162 ± 81
227 $\mu\text{g}/\text{m}^3$ in 2011 to $60 \pm 41 \mu\text{g}/\text{m}^3$ in 2022, representing a reduction of approximately 63%. In particular,
228 the reduction rate reached 72% after 2013. As for chemical components, the largest reductions were
229 observed in SO_4^{2-} (79%), decreasing from $38.0 \pm 19.9 \mu\text{g}/\text{m}^3$ in 2013 to $7.9 \pm 4.5 \mu\text{g}/\text{m}^3$ in 2022,
230 followed by EC (76%). Additionally, the concentrations of NH_4^+ and NO_3^- also significantly decreased
231 by 68% and 56%, respectively. The proportion of each component in PM_{2.5} (Fig. S3) reveals a decrease
232 in SO_4^{2-} , K^+ , and Cl^- , indicating effective control measures targeting coal and biomass combustion
233 (Lei et al., 2021). However, the proportions of NO_3^- and OC in PM_{2.5} rose from 11% and 12% in 2013
234 to 13% and 17% in 2022, respectively, similar to the trend observed in the North China Plain (Wen et
235 al., 2018; Zhai et al., 2019; Li et al., 2023).

236 3.2 Temporal variations in CM

237 Notably, there is no clear declining trend in the CM concentration, with a rebound observed during
238 2020–2022 (Fig. 1i). Furthermore, the proportion of CM in PM_{2.5} exhibits a significant upward trend
239 (Fig. S3). To further analyze its trend, sampling data were divided into three periods corresponding to
240 governmental stages: 2011–2013, when no special control measures were implemented; 2013–2019,

241 coinciding with the implementation of the Air Pollution Prevention and Control Action Plan; and
 242 2019–2022, coinciding with the Three-Year Action Plan. During these periods, Henan Province and
 243 Zhengzhou City implemented several dust control policies summarized in Table S3. As shown in Fig.
 244 2a and 2b, the mass concentration of CM peaked at $14.6 \pm 8.3 \mu\text{g}/\text{m}^3$ in 2013, accounting for 8% of
 245 $\text{PM}_{2.5}$. To evaluate the inter - annual change trend of CM, the Mann - Kendall method, Sen's slope,
 246 and Least - Squares (LS) slope were comprehensively used with the results presented in Table S4.
 247 From 2013 to 2019, the CM concentration notably decreased from 14.6 ± 8.3 to $8.5 \pm 7.8 \mu\text{g}/\text{m}^3$, with
 248 an annual average decline rate of $0.81 \mu\text{g}/(\text{m}^3 \cdot \text{year})$ from LS slope [$0.015 \mu\text{g}/(\text{m}^3 \cdot \text{year})$ from Sen's
 249 slope]. Apart from control measures, the interannual meteorological analysis shows (Fig. S4) WS
 250 exhibited a declining trend, with a decrease rate of 43%, while RH showed an increasing trend at a rate
 251 of 8% from 2013 to 2019, under which conditions that were unfavorable for dust resuspension (Wang
 252 et al., 2013, 2018). Seasonal trends (Fig. S5) reveal significant declines in CM during spring in 2013–
 253 2019 with WS decreasing from 2.2 m/s in 2013 to 1.4 m/s in 2019 (Fig. S6) and stable RH (Fig. S7).
 254 Similarly, summer CM reductions in 2013–2019 corresponded with WS declines. These patterns
 255 suggest spring-summer CM improvements resulted from the synergistic effects of meteorological
 256 changes and dust control policies. Conversely, autumn-winter seasons showed limited CM reductions
 257 despite comparable WS decreases in 2013–2019, highlighting the need for enhanced dust emission
 258 controls in Zhengzhou during these seasons. As for the individual crustal elements in Fig. S8, Ca
 259 exhibited the highest average annual decline rate of 33% during 2013–2019, followed by Al. Si showed
 260 a less pronounced decline, attributed to its association with soil dust, where control measures for
 261 exposed soil are lacking (Zhang et al., 2020). In addition, the Ca^{2+} concentration as depicted in Fig. 2c

decreased from $3.2 \pm 2.1 \mu\text{g}/\text{m}^3$ in 2013 to $2.2 \pm 1.1 \mu\text{g}/\text{m}^3$ in 2019, with an approximate annual average decline rate of $0.32 \mu\text{g}/(\text{m}^3 \cdot \text{year})$ from LS slope [$4.14\text{E}-03 \mu\text{g}/(\text{m}^3 \cdot \text{year})$ from Sen's slope] in Table S4, further demonstrating the decline in dust source. It was worth noting that the proportions of CM, Ca, Al, Fe, Si, and Ca^{2+} in $\text{PM}_{2.5}$ have shown consecutive annual increases from 2013 to 2019, with CM proportion increasing from 8% in 2013 to 14% in 2019, indicating that CM reduction lagged behind $\text{PM}_{2.5}$ reduction efforts in Zhengzhou during this period. Additionally, both concentration and proportion of Ca^{2+} in 2022 ($2.2 \pm 1.1 \mu\text{g}/\text{m}^3$ and 14%) were higher than in other cities of China, such as Beijing ($1.0 \mu\text{g}/\text{m}^3$ and 2.8%), Tianjin ($0.5 \mu\text{g}/\text{m}^3$ and 1.4%), and Xiamen ($0.48 \mu\text{g}/\text{m}^3$ and 1.5%) (Shi et al., 2017; Xu et al., 2025; Zhang et al., 2021). These results indicate that CM remained an important component of $\text{PM}_{2.5}$ in Zhengzhou City.

During 2019–2022, both CM and Ca^{2+} concentrations exhibited significant rebounds, with annual growth rates of 0.24 and $0.4 \mu\text{g}/(\text{m}^3 \cdot \text{year})$ from LS slope [$5.80\text{E}-03$ and $5.42\text{E}-03 \mu\text{g}/(\text{m}^3 \cdot \text{year})$ from Sen's slope], respectively, and their proportions increased from 14% and 2% in 2019 to 22% and 5% in 2022. CM concentrations rebounded in all seasons, particularly in winter (Fig. S5). Changes in meteorological conditions may be a significant factor contributing to these concentration rebounds, accompanied by the average WS increased by 0.14 m/s and RH decreased by 7% from 2020 to 2022 (Fig. S4, S6, and S7), facilitating dust resuspension. Furthermore, the lack of more effective dust control measures, as indicated by the absence of significant changes in the dust control policies from the Air Pollution Prevention and Control Action Plan and Three-Year Action Plan, may be another important factor contributing to the rebound of dust.

3.3 Sources of CM

Elemental ratios were employed to characterize the sources of CM, with the Ca/Al ratio widely recognized as a reliable indicator of sandy origin (Zhang et al., 2017). In addition, significant variations in Ca/Si ratios (Table S5) were observed among different dust sources (Road, Construction, Piles, Soil). Fig. 3a illustrates the trend in Ca/Si ratios from 2011 to 2022. After 2013, Ca/Si ratios showed a declining trend annually, with the average ratio decreasing from a peak of 1.6 in 2016 to a lowest of 0.4 in 2022. Compared with Ca/Si ratios from different types of dust sources, the effect of road and construction dust on CM has gradually decreased. This may be attributed to the implementation of dust control measures such as enclosure, shielding, and dust suppression at construction and demolition sites, as well as dust control on ground surfaces and roads (Table S5). During 2019–2022, the average Ca/Si ratio remained below 1, with a mean of 0.4 in 2022, indicating that soil dust predominantly contributed to CM. Currently, measures for controlling soil-suspended dust are limited, primarily relying on long-term strategies such as afforestation and increasing urban green coverage, thus requiring a longer process and sustained investment.

Sand dust transport serves as a significant source of CM in the North China Plain (Zhang et al., 2024). The Ca/Al ratio from 2016 to 2022 (Fig. 3b) shows minimal variation, with annual averages ranging between 1.5 and 2.5, indicating no significant changes in the source regions of sand. The transport trajectories reveal that the predominant pathways for long-distance transport of sand dust originated from Inner Mongolia, passing through Shaanxi and Shanxi provinces. Compared to 2013–2018 (45%), the influence of long-distance transport decreased to 25% during 2019–2022. In contrast, local transport within Henan province and short-distance transport from Shandong province showed a

noticeable increase. These findings suggest that the rebound in CM concentrations during 2019–2022 in Zhengzhou might be responsible for the resuspension of surrounding soil dust.

3.4 Long-term trend of particle pH

Are shown in Fig. 4 and Table S4, pH values showed a clearly increasing trend after 2014. From 2013 to 2019, the annual pH increased by 0.11 units from the LS slope [$9.15\text{E-}04$ units from Sen's slope], reaching a maximum median value of 4.45 (Mean: 4.35) in 2018. Note that the annual average growth rate of pH values increased to 0.21 units from LS slope [$2.93\text{E-}03$ units from Sen's slope] from 2019 to 2022, with a maximum median value of 4.42 (Mean: 4.51) in 2022. Seasonally, pH values showed increasing trends in spring, summer, and autumn, and notably increased in winter from 2020 to 2022 (Fig. S9). The increasing trend in pH values observed in this study is similar to the findings in Beijing (Song et al., 2019; Xie et al., 2020), presumably attributable to the comparable chemical composition trends and meteorological conditions. In contrast, Shanghai and Hong Kong display divergent trends (Nah et al., 2023; Zhou et al., 2022). This disparity might be ascribed to the stronger buffering effect exerted by NH_3 and dust in Zhengzhou than marine aerosols (Na^+/Cl^-) in these coastal cities (Shi et al., 2017; Liu et al., 2019). Moreover, the relatively higher temperatures and more abundant rainfall in Shanghai and Hong Kong could also contribute to the distinct trends observed in their pH values.

Sensitivity analyses were conducted to explore the dominant factors driving the elevated particle pH in Zhengzhou by giving a range for one parameter (i.e., TNH_x) and average values for other parameters (i.e., SO_4^{2-} , NO_3^- , Na^+ , Cl^- , Ca^{2+} , K^+ , Mg^{2+} , RH, and T) input into the ISORROPIA-II model.

Are shown in Fig. S10, particle pH increases with the cation concentrations (e.g., TNH_x , K^+ , Ca^{2+} , Mg^{2+} , and Na^+) and decreases with anions concentrations (e.g., SO_4^{2-} and NO_3^-). Additionally, RH does not significantly affect pH, whereas an increase in T leads to a noticeable decrease in particle pH.

Based on the sensitivity analysis curves, the pH values corresponding to a variable in different years were calculated according to the average values of this variable in different years (Table S6). The difference in pH values of this variable between two adjacent years was defined as ΔpH which is illustrated in Fig. 5. According to Equation (2), in addition to H^+ concentration, particle pH is primarily influenced by the dilution effect of ALWC. Moreover, ALWC affects the gas-particle partitioning of semi-volatile compounds, thereby influencing particle acidity (Zuend et al., 2010; Zuend and Seinfeld, 2012). As shown in Fig.5 and Table S6, only in 2015, 2019, and 2020 did the increases in ALWC concentration ($17.6 \mu\text{g}/\text{m}^3$, $4.1 \mu\text{g}/\text{m}^3$, and $11.6 \mu\text{g}/\text{m}^3$, respectively) lead to pH increases of 0.22, 0.06, and 0.14 units. This clearly cannot fully explain the significant pH increase in Zhengzhou since 2013. Notably, since 2013, H^+ concentration has shown a decreasing trend. Particularly, H^+ concentrations decreased by 7.6×10^{-6} , 11.2×10^{-6} , and $7.2 \times 10^{-6} \text{ mol/L}$ in 2013, 2015, and 2017, respectively, leading to pH increases of 0.21, 0.36, and 0.42 units. After 2019, a continuous decline in H^+ concentration was observed for three consecutive years, resulting in pH increases of 0.21, 0.13, and 0.2 units in 2020, 2021, and 2022, respectively. These findings indicate that the increase in pH from 2019 to 2022 in Zhengzhou was primarily driven by the reduction in H^+ concentration.

The concentration of H^+ in the aerosol liquid phase is influenced by both chemical composition and meteorological conditions. To further understand the factors affecting ΔpH , we analyzed the variations in $\text{PM}_{2.5}$ chemical components and meteorological parameters. Results indicate that the

decline in SO_4^{2-} from 2013 to 2018 was the primary cause of the increase in particle pH, as it decreased H^+ and ALWC concentrations (Fig. S11) in aerosol (Ding et al., 2019; Zhang et al., 2021). The average SO_4^{2-} concentration decreased by 14.6 and 5.3 $\mu\text{g}/\text{m}^3$, resulting in a pH increase of 0.43 and 0.35 units from 2013 to 2014 and 2016 to 2017, respectively, which was comparable to an increased rate of 0.3 units in East Asia due to SO_2 emission controls since 2016 (Karydis et al., 2021). As another acidic ion, the decrease in nitrate concentration did not significantly contribute to the pH increases, consistent with findings from Ding et al. (2019) and Zhang et al. (2021). This is primarily because NO_3^- declined more slowly compared to sulfate ions and exceeded sulfate concentrations after 2016, under which conditions that nitrate-rich particles can absorb twice the amount of water that sulfate-rich particles, leading to an increase in ALWC concentration and inhibiting pH decline (Lin et al., 2020; Xie et al., 2020). On the other hand, increases in particle pH in 2015 and 2018 were notably influenced by changes in TNH_x with concentrations increased by 5.5 and 1.3 $\mu\text{g}/\text{m}^3$, respectively. Increased TNH_x concentrations could react with SO_4^{2-} or NO_3^- and consume a substantial amount of H^+ , thereby raising particulate matter pH values (Seinfeld et al., 1998; Zhang et al., 2021). Substantial decreases in T in 2015 (4.2°C), 2017 (4.9°C), and 2018 (2.8°C), favoring NH_3 partitioning into the particle phase and reducing H^+ concentrations, drove increases in particle pH (Tao and Murphy, 2019).

During the period from 2020 to 2022, the influence of SO_4^{2-} on particle pH gradually decreased, with a decrease in concentration from 0.3 to 2.3 $\mu\text{g}/\text{m}^3$ (Table S6) only bringing about a pH decrease of 0.03 to 0.14 (Fig. 5). Moreover, a rebound in SO_4^{2-} concentration to $7.9 \pm 4.5 \mu\text{g}/\text{m}^3$ in 2022 even resulted in a decrease of 0.11 units in pH instead. On the other hand, TNH_x began to show a slight annual decline (0.9 to 2.2 $\mu\text{g}/\text{m}^3$), resulting in a significant decrease in pH (0.21–0.35). Consequently,

the increase in pH values was closely related to the rise in Ca^{2+} concentration. Ca^{2+} is less volatile and competes preferentially with NH_3 to neutralize anions such as SO_4^{2-} to form insoluble CaSO_4 , which precipitates from the aerosol aqueous phase (Ding et al., 2019; Karydis et al., 2021), thereby reducing H^+ concentrations (Fig. S11) and subsequently lowering particle acidity. Specifically, increases of 0.7 and $0.5 \mu\text{g}/\text{m}^3$ in Ca^{2+} concentrations led to pH increases of 0.13 and 0.09 units in 2020 and 2022, respectively, making Ca^{2+} a primary controlling factor for pH elevation.

4 Conclusions

The annual average $\text{PM}_{2.5}$ concentration in Zhengzhou decreased from $212.4 \pm 101.5 \mu\text{g}/\text{m}^3$ in 2013 to $59.5 \pm 41.2 \mu\text{g}/\text{m}^3$ in 2022, with the largest reduction in SO_4^{2-} . As for CM, their concentrations notably decreased from 2013 to 2019, because of effective dust control measures, as well as decreased wind speed and increased relative humidity. However, the proportions of CM in $\text{PM}_{2.5}$ have shown consecutive annual increases. In addition, CM concentrations and their proportions increased significantly during 2019–2022, which might be responsible for the resuspension of surrounding soil dust. Correspondingly, the annual pH increased by 0.11 units from 2013 to 2019 mainly due to the decline in SO_4^{2-} , increased TNH_x , or decreased temperature. During the period from 2020 to 2022, the annual average growth rate of pH values increased to 0.21 units from 2019 to 2022, which was determined by the rise in Ca^{2+} concentration.

5 Implication

Control measures implemented by the Chinese government have proven effective in reducing dust, but this study reveals that the crustal materials in $\text{PM}_{2.5}$ rebounded after 2019. This phenomenon is not unique to Zhengzhou, as major cities in the North China Plain have also experienced a pronounced upward trend in coarse particles after 2019 (Fig. S12). Thus, crustal materials persist as a substantial constituent of atmospheric aerosols in North China, sustaining elevated particle pH levels. Extensive research has established that heightened particle pH inhibits nitrate reduction in aerosols (Ding et al., 2019; Lin et al., 2020; Wen et al., 2018), particularly significant given nitrate's predominant role in haze formation within this region. Notably, while moderately acidic aerosols demonstrate reduced health impacts, particles with $\text{pH} < 3$ exhibit substantially greater health risks (Shi et al., 2019). Consequently, future environmental management strategies must prioritize real-time assessment of regulatory impacts on particle acidity. This necessitates an integrated approach that simultaneously addresses acidic precursors, alkaline precursors, and crustal material contributions to atmospheric acid chemistry.

Data availability

All the data presented in this article can be accessed through <https://doi.org/10.5281/zenodo.14032007> (Zhang, 2024).

399 **Supporting Information**

400 Additional data, figures, and tables, some of which are referenced directly within the manuscript,
401 and detailed descriptions of field measurements and samples.

402 **Author contributions**

403 S.W. designed this study. H.Z. and Z.D. analyzed the data and prepared the manuscript with the
404 contributions of all coauthors. X.L. conducted measurements. R.Z. provided funding acquisition. All
405 authors have read and agreed to the published version of the manuscript.

406 **Competing interests**

407 The authors declare that they have no conflict of interest.

408 **Acknowledgment**

409 This work was supported by the National Key Research and Development Program of China (No.
410 2024YFC3713701), the China Postdoctoral Science Foundation (2023 M733220), the Zhengzhou
411 PM_{2.5} and O₃ Collaborative Control and Monitoring Project (20220347 A), and the National Key R&D
412 Program of China No. 2017YFC0212400.

Funding Sources

This work was supported by the National Key Research and Development Program of China (No. 2024YFC3713701), the China Postdoctoral Science Foundation (2023 M733220), the Zhengzhou PM_{2.5} and O₃ Collaborative Control and Monitoring Project (20220347 A), and the National Key Research and Development Program of China (No. 2017YFC0212400).

References

- Battaglia, M. A.; Douglas, S.; Hennigan, C.: Effect of the urban heat island on aerosol pH, *Environ. Sci. Technol.*, 51, 13095–13103, <https://doi.org/10.1021/acs.est.7b02786>, 2017.
- Chang, R. Y. W.; Slowik, J. G.; Shantz, N. C.; Vlasenko, A.; Liggio, J.; Sjostedt, S. J.; Leaitch, W. R.; Abbatt, J. P. D. The hygroscopicity parameter (κ) of ambient organic aerosol at a field site subject to biogenic and anthropogenic influences: relationship to degree of aerosol oxidation. *Atmos. Chem. Phys.*, 10, 5047–5064, <https://doi.org/10.5194/acp-10-5047-2010>, 2010.
- Ding, J., Zhao, P., Su, J., Dong, Q., Du, X., and Zhang, Y.: Aerosol pH and its driving factors in Beijing, *Atmos. Chem. Phys.*, 19, 7939–7954, <https://doi.org/10.5194/acp-19-7939-2019>, 2019.
- Dong, J., Li, B., Li, Y., Zhou, R., Gan, C., Zhao, Y., Liu, R., Yang, Y., Wang, T., and Liao, H.: Atmospheric ammonia in China: Long-term spatiotemporal variation, urban-rural gradient, and influencing factors, *Sci. Total Environ.*, 883, 163733, <https://doi.org/10.1016/j.scitotenv.2023.163733>, 2023.
- Fountoukis, C and Nenes, A.: ISORROPIA II: a computationally efficient thermodynamic equilibrium model for K^+ - Ca^{2+} - Mg^{2+} - NH_4^+ - Na^+ - SO_4^{2-} - NO_3^- - Cl^- - H_2O aerosols, *Atmos. Chem. Phys.*, 7, 4639–4659, <https://doi.org/10.5194/acp-7-4639-2007>, 2007.
- Guo, H., Sullivan, A. P., Campuzano-Jost, P., Schroder, J. C., Lopez-Hilfiker, F. D., Dibb, J. E., Jimenez, J. L., Thornton, J. A., Brown, S. S., Nenes, A., and Weber, R. J.: Fine particle pH and the

partitioning of nitric acid during winter in the northeastern United States, *J. Geophys. Res. Atmos.*, 121, 10,355–310,376, <https://doi.org/10.1002/2016JD025311>, 2016.

Guo, H., Xu, L., Bougiatioti, A., Cerully, K. M., Capps, S. L., Hite Jr, J. R., Carlton, A. G., Lee, S. H., Bergin, M. H., Ng, N. L., Nenes, A., and Weber, R. J.: Fine-particle water and pH in the southeastern United States, *Atmos. Chem. Phys.*, 15, 5211–5228, <https://doi.org/10.5194/acp-15-5211-2015>, 2015.

Heald, C.; Collett, J. J.; Lee, T.; Benedict, K.; Schwandner, F.; Li, Y.; Clarisse, L.; Hurtmans, D. R.; Van, D. M.; Clerbaux, C.; Coheur, P. F., Philip, S.; Martin, R. V.; Pye, T.: Atmospheric ammonia and particulate inorganic nitrogen over the United States, *Atmos. Chem. Phys.*, 12, 10295–10312, <https://doi.org/10.5194/acp-12-10295-2012>, 2012.

Huang, X., Song, Y., Li, M., Li, J., Huo, Q., Cai, X., Zhu, T., Hu, M., and Zhang, H.: A high-resolution ammonia emission inventory in China, *Global. Biogeochem. Cy.*, 26, GB1030, <https://doi.org/10.1029/2011GB004161>, 2012.

Jiang, N.; Duan, S.; Yu, X.; Zhang, R.; Wang, K. Comparative major components and health risks of toxic elements and polycyclic aromatic hydrocarbons of PM_{2.5} in winter and summer in Zhengzhou: Based on three-year data. *Atmos. Res.*, 213, 173–184, <https://doi.org/10.1016/j.atmosres.2018.06.008>, 2018.

Karydis, V. A., Tsimpidi, A. P., Pozzer, A., and Lelieveld, J.: How alkaline compounds control atmospheric aerosol particle acidity, *Atmos. Chem. Phys.*, 21, 14983–15001, <https://doi.org/10.5194/acp-21-14983-2021>, 2021.

Kim, Y., Park, O., Park, S. H., Kim, M. J., Kim, J.-J., Choi, J.-Y., Lee, D., Cho, S., and Shim, S.: PM_{2.5} pH estimation in Seoul during the KORUS-AQ campaign using different thermodynamic models, *Atmos. Environ.*, 268, 118787, <https://doi.org/10.1016/j.atmosenv.2021.118787>, 2022.

Lei, L., Zhou, W., Chen, C., He, Y., Li, Z., Sun, J., Tang, X., Fu, P., Wang, Z., and Sun, Y.: Long-term characterization of aerosol chemistry in cold season from 2013 to 2020 in Beijing, China, *Environ. Pollut.*, 268, 115952, <https://doi.org/10.1016/j.envpol.2020.115952>, 2021.

Li, C.; Hu, Y.; Chen, J.; Ma, Z.; Ye, X.; Yang, X.; Wang, L.; Wang, X.; Mellouki, A. Physiochemical

properties of carbonaceous aerosol from agricultural residue burning: Density, volatility, and hygroscopicity. *Atmos. Environ.*, 140, 94–105, <https://doi.org/10.1016/j.atmosenv.2016.05.052>, 2016.

Li, W., Xu, L., Liu, X., Zhang, J., Lin, Y., Yao, X., Gao, H., Zhang, D., Chen, J., Wang, W., Harrison, R. M., Zhang, X., Shao, L., Fu, P., Nenes, A., and Shi, Z.: Air pollution-aerosol interactions produce more bioavailable iron for ocean ecosystems, *Sci. Adv.*, 3, e1601749, <https://doi.org/10.1126/sciadv.1601749>, 2017.

Li, Y., Lei, L., Sun, J., Gao, Y., Wang, P., Wang, S., Zhang, Z., Du, A., Li, Z., Wang, Z., Kim, J. Y., Kim, H., Zhang, H., and Sun, Y.: Significant reductions in secondary aerosols after the Three-Year Action Plan in Beijing summer, *Environ. Sci. Technol.*, 57, 15945–15955, <https://doi.org/10.1021/acs.est.3c02417>, 2023.

Lin, Y., Zhang, Y., Fan, M., and Bao, M.: Heterogeneous formation of particulate nitrate under ammonium-rich regimes during the high-PM_{2.5} events in Nanjing, China, *Atmos. Chem. Phys.*, 20, 3999–4011, <https://doi.org/10.5194/acp-20-3999-2020>, 2020.

Liu, M.; Huang, X.; Song, Y.; Tang, J.; Cao, J.; Zhang, X.; Zhang, Q.; Wang, S.; Xu, T.; Kang, L.; Gai, X.; Zhang, H.; Yang, F.; Wang, H.; Yu, J.; Lau, A.; He, L.; Huang, X.; Duan, L.; Ding, A.; Xue, L.; Gao, J.; Liu, B.; Zhu, T. Ammonia emission control in China would mitigate haze pollution and nitrogen deposition, but worsen acid rain. *Proc. Natl. Acad. Sci.*, 116, 7760–7765, <https://doi.org/10.1073/pnas.1814880116>, 2019.

Liu, Z., Gao, W., Yu, Y., Hu, B., Xin, J., Sun, Y., Wang, L., Wang, G., Bi, X., Zhang, G., Xu, H., Cong, Z., He, J., Xu, J., and Wang, Y.: Characteristics of PM_{2.5} mass concentrations and chemical species in urban and background areas of China: emerging results from the CARE-China network, *Atmos. Chem. Phys.*, 18, 8849–8871, <https://doi.org/10.5194/acp-18-8849-2018>, 2018.

Mao, I., Lin, C., Lin, C., Chen, Y., Sung, F., and Chen, M.: Exposure of acid aerosol for schoolchildren in metropolitan Taipei, *Atmos. Environ.*, 43, 5622–5629, <https://doi.org/10.1016/j.atmosenv.2009.07.054>, 2009.

Masiol, M., Squizzato, S., Formenton, G., Khan, M. B., Hopke, P. K., Nenes, A., Pandis, S. N., Tositti,

490 L., Benetello, F., Visin, F., and Pavoni, B.: Hybrid multiple-site mass closure and source
 491 apportionment of PM_{2.5} and aerosol acidity at major cities in the Po Valley, *Sci. Total Environ.*,
 492 704, 135287, <https://doi.org/10.1016/j.scitotenv.2019.135287>, 2020.
 493 MEP (Ministry of Environment Protection), 2023. [https://www.mee.gov.cn/ywdt/hjywnews/2024](https://www.mee.gov.cn/ywdt/hjywnews/202406/t20240605_1075031.shtml)
 494 [06/t20240605_1075031.shtml](https://www.mee.gov.cn/ywdt/hjywnews/202406/t20240605_1075031.shtml), Accessed date:5 June 2024.
 495 Nah, T., Lam, Y. H., Yang, J., and Yang, L.: Long-term trends and sensitivities of PM_{2.5} pH and aerosol
 496 liquid water to chemical composition changes and meteorological parameters in Hong Kong,
 497 South China: Insights from 10-year records from three urban sites, *Atmos. Environ.*, 302,
 498 <https://doi.org/10.1016/j.atmosenv.2023.119725>, 2023.
 499 Nenes, A., Pandis, S. N., Kanakidou, M., Russell, A. G., Song, S., Vasilakos, P., and Weber, R. J.:
 500 Aerosol acidity and liquid water content regulate the dry deposition of inorganic reactive nitrogen,
 501 *Atmos. Chem. Phys.*, 21, 6023–6033, <https://doi.org/10.5194/acp-21-6023-2021>, 2021.
 502 Pinder, R., Adams, P., and Pandis, S.: Ammonia emission controls as a cost-effective strategy for
 503 reducing atmospheric particulate matter in the eastern United States, *Environ. Sci. Technol.*, 41,
 504 380–386, <https://doi.org/10.1021/es060379a>, 2007.
 505 Pinder, R., Gilliland, A., and Dennis, R.: Environmental impact of atmospheric NH₃ emissions under
 506 present and future conditions in the eastern United States, *Geophys. Res. Lett.*, 35, 28,
 507 <https://doi.org/10.1029/2008gl033732>, 2008.
 508 Pye, H. O. T.; Nenes, A.; Alexander, B.; Ault, A. P.; Barth, M. C.; Clegg, S. L.; Collett Jr, J. L.; Fahey,
 509 K. M.; Hennigan, C. J.; Herrmann, H.; Kanakidou, m.; Kelly, J. T.; Ku, L.; McNeill, V. F.; Riemer,
 510 N.; Schaefer, T.; Shi, G.; Tilgner, A.; Walker, J.T.; Wang, T.; Weber, R.; Xing, J.; Zaveri, R. A.;
 511 Zuend, A. The acidity of atmospheric particles and clouds. *Atmos. Chem. Phys.*, 20, 4809–4888,
 512 <https://doi.org/10.5194/acp-20-4809-2020>, 2020.
 513 Rengarajan, R., Sudheer, A. K., and Sarin, M. M.: Aerosol acidity and secondary organic aerosol
 514 formation during wintertime over urban environment in western India, *Atmos. Environ.*, 45,
 515 1940–1945, <https://doi.org/10.1016/j.atmosenv.2011.01.026>, 2011.
 516 Seinfeld, J. H., Pandis, S. N., and Noone, K. J.: Atmospheric chemistry and physics: From air pollution

517 to climate change, *Phys. Today.*, 51, 88–90, <https://doi.org/10.1063/1.882420>, 1998.

518 Sharma, B., Jia, S., Polana, A. J., Ahmed, M. S., Haque, R. R., Singh, S., Mao, J., and Sarkar, S.:
 519 Seasonal variations in aerosol acidity and its driving factors in the eastern Indo-Gangetic Plain:
 520 A quantitative analysis, *Chemosphere.*, 305, 135490,
 521 <https://doi.org/10.1016/j.chemosphere.2022.135490>, 2022.

522 Shi, G., Xu, J., Peng, X., Xiao, Z., Chen, K., Tian, Y., Guan, X., Feng, Y., Yu, H., Nenes, A., and Russell,
 523 A. G.: pH of aerosols in a polluted atmosphere: source contributions to highly acidic aerosol,
 524 *Environ. Sci. Technol.*, 51, 4289–4296, <https://doi.org/10.1021/acs.est.6b05736>, 2017.

525 Shi, X., Nenes, A., Xiao, Z., Song, S., Yu, H., Shi, G., Zhao, Q., Chen, K., Feng, Y., and Russell, A.
 526 G.: High-resolution data sets unravel the effects of sources and meteorological conditions on
 527 nitrate and its gas-particle partitioning, *Environ. Sci. Technol.*, 53, 3048–3057,
 528 <https://doi.org/10.1021/acs.est.8b06524>, 2019.

529 Song, S., Nenes, A., Gao, M., Zhang, Y., Liu, P., Shao, J., Ye, D., Xu, W., Lei, L., Sun, Y., Liu, B.,
 530 Wang, S., and McElroy, M. B.: Thermodynamic modeling suggests declines in water uptake and
 531 acidity of inorganic aerosols in Beijing winter haze events during 2014/2015–2018/2019, *Environ.*
 532 *Sci. Technol. Lett.*, 6, 752–760, <https://doi.org/10.1021/acs.estlett.9b00621>, 2019.

533 Su, H., Cheng, Y., and Pöschl, U.: New Multiphase Chemical Processes Influencing Atmospheric
 534 Aerosols, Air Quality, and Climate in the Anthropocene, *Acc. Chem. Res.*, 53, 2034–2043,
 535 <https://doi.org/10.1021/acs.accounts.0c00246>, 2020.

536 Surratt, J. D., Chan, A. W. H., Eddingsaas, N. C., Chan, M., Loza, C. L., Kwan, A. J., Hersey, S. P.,
 537 Flagan, R. C., Wennberg, P. O., and Seinfeld, J. H.: Reactive intermediates revealed in
 538 secondary organic aerosol formation from isoprene, *Proc. Natl. Acad. Sci.*, 107, 6640–6645,
 539 <https://doi.org/10.1073/pnas.0911114107>, 2010.

540 Tao, Y. and Murphy, J. G.: The sensitivity of PM_{2.5} acidity to meteorological parameters and chemical
 541 composition changes: 10-year records from six Canadian monitoring sites, *Atmos. Chem. Phys.*,
 542 19, 9309–9320, <https://doi.org/10.5194/acp-19-9309-2019>, 2019.

543 Tian, Y.; Chen, G.; Wang, H.; Huang-Fu, Y.; Shi, G.; Han, B.; and Feng, Y.: Source regional

544 contributions to PM_{2.5} in a megacity in China using an advanced source regional apportionment
 545 method. *Chemosphere.*, 147, 256–263, <https://doi.org/10.1016/j.chemosphere.2015.12.132>, 2016.
 546 Tremper, A.; Font, A.; Priestman, M.; Hamad, S.; Chung, T.; Pribadi, A.; Brown, R.; Goddard, S.;
 547 Grassineau, N.; Petterson, K.; Kelly, F.; Green, D.: Field and laboratory evaluation of a high time
 548 resolution x-ray fluorescence instrument for determining the elemental composition of ambient
 549 aerosols, *Atmos. Meas. Tech.*, 11, 3541–3557, <https://doi.org/10.5194/amt-11-3541-2018>, 2018.
 550 Wang, C., Yin, S., Bai, L., Zhang, X., Gu, X., Zhang, H., Lu, Q., and Zhang, R.: High-resolution
 551 ammonia emission inventories with comprehensive analysis and evaluation in Henan, China,
 552 2006–2016, *Atmos. Environ.*, 193, 11–23, <https://doi.org/10.1016/j.atmosenv.2018.08.063>, 2018.
 553 Wang, G., Chen, J., Xu, J., Yun, L., Zhang, M., Li, H., Qin, X., Deng, C., Zheng, H., Gui, H., Liu, J.,
 554 and Huang, K.: Atmospheric processing at the Sea-Land interface over the South China Sea:
 555 Secondary aerosol formation, aerosol acidity, and role of sea salts, *J. Geophys. Res. Atmos.*,
 556 127, <https://doi.org/10.1029/2021jd036255>, 2022.
 557 Wang, L., Du, H., Chen, J., Zhang, M., Huang, X., Tan, H., Kong, L., and Geng, F.: Consecutive
 558 transport of anthropogenic air masses and dust storm plume: Two case events at Shanghai, China,
 559 *Atmos. Res.*, 127, 22–33, <https://doi.org/10.1016/j.atmosres.2013.02.011>, 2013.
 560 Wang, S., Yin, S., Zhang, R., Yang, L., Zhao, Q., Zhang, L., Yan, Q., Jiang, N., and Tang, X.: Insight
 561 into the formation of secondary inorganic aerosol based on high-time-resolution data during haze
 562 episodes and snowfall periods in Zhengzhou, China, *Sci. Total Environ.*, 660, 47–56,
 563 <https://doi.org/10.1016/j.scitotenv.2018.12.465>, 2019.
 564 Wang, S.; Wang, L.; Li, Y.; Wang, C.; Wang, W.; Yin, S.; Zhang, R.; Effect of ammonia on fine-particle
 565 pH in agricultural regions of China: comparison between urban and rural sites, *Atmos. Chem.*
 566 *Phys.*, 20, 2719–2734, <https://doi.org/10.5194/acp-20-2719-2020>, 2020.
 567 Wang, Y. Q., Zhang, X. Y., and Draxler, R. R.: TrajStat: GIS-based software that uses various trajectory
 568 statistical analysis methods to identify potential sources from long-term air pollution
 569 measurement data, *Environ. Model. Softw.*, 24, 938–939,
 570 <https://doi.org/10.1016/j.envsoft.2009.01.004>, 2009.

Wang, Z., Pan, X., Uno, I., Chen, X., Yamamoto, S., Zheng, H., Li, J., and Wang, Z.: Importance of mineral dust and anthropogenic pollutants mixing during a long-lasting high PM event over East Asia, *Environ. Pollut.*, 234, 368–378, <https://doi.org/10.1016/j.envpol.2017.11.068>, 2018.

Weber, R.; Guo, H.; Russell, A.; Nenes, A.: High aerosol acidity despite declining atmospheric sulfate concentrations over the past 15 years, *Nature Geoscience.*, 9, 282–285, <https://doi.org/10.1038/ngeo2665>, 2016.

Wei, Y.; Wang, S.; Jiang, N.; Zhang, R.; and Hao, Q. Comparative multi-model study of PM_{2.5} acidity trend changes in ammonia-rich regions in winter: Based on a new ammonia concentration assessment method, *J. Hazard.*, 458, 15, <https://doi.org/10.1016/j.jhazmat.2023.131970>, 2023.

Wen, L., Xue, L., Wang, X., Xu, C., Chen, T., Yang, L., Wang, T., Zhang, Q., and Wang, W.: Summertime fine particulate nitrate pollution in the North China Plain: increasing trends, formation mechanisms and implications for control policy, *Atmos. Chem. Phys.*, 18, 11261–11275, <https://doi.org/10.5194/acp-18-11261-2018>, 2018.

Wexler, A. S. and Seinfeld, J. H.: Second-generation inorganic aerosol model, *Atmos. Environ., Part A. General Topics*, 25, 2731–2748, [https://doi.org/10.1016/0960-1686\(91\)90203-J](https://doi.org/10.1016/0960-1686(91)90203-J), 1991.

Xie, Y., Wang, G., Wang, X., Chen, J., Chen, Y., Tang, G., Wang, L., Ge, S., Xue, G., Wang, Y., and Gao, J.: Nitrate-dominated PM_{2.5} and elevation of particle pH observed in urban Beijing during the winter of 2017, *Atmos. Chem. Phys.*, 20, 5019–5033, <https://doi.org/10.5194/acp-20-5019-2020>, 2020.

Xu, K., Yin, L., Chen, Q., Liao, D., Ji, X., Zhang, K., Wu, Y., Xu, L., Li, M., Fan, X., Zhang, F., Huang, Z., Chen, J., and Hong, Y.: Quantitative analysis of influencing factors to aerosol pH and its responses to PM_{2.5} and O₃ pollution in a coastal city, *J. Environ. Sci.*, 151, 284–297, <https://doi.org/10.1016/j.jes.2024.03.044>, 2025.

Yu, F., Yan, Q., Jiang, N., Su, F., Zhang, L., Yin, S., Li, Y., Zhang, R., and Chen, L.: Tracking pollutant characteristics during haze events at background site Zhongmu, Henan Province, China, *Atmos. Pollut. Res.*, 8, 64–73, <https://doi.org/10.1016/j.apr.2016.07.005>, 2017.

598 Zhai, S.; Jacob, D.J.; Wang, X.; Shen, L.; Li, K.; Zhang, Y.; Gui, K.; Zhao, T.; Liao, H. Fine particulate
 599 matter (PM_{2.5}) trends in China, 2013–2018: separating contributions from anthropogenic
 600 emissions and meteorology, *Atmos. Chem. Phys.*, 19, 11031–11041, [https://doi.org/10.5194/acp-](https://doi.org/10.5194/acp-19-11031-2019)
 601 [19-11031-2019](https://doi.org/10.5194/acp-19-11031-2019), 2019.

602 Zhang, B., Shen, H., Liu, P., Guo, H., Hu, Y., Chen, Y., Xie, S., Xi, Z., Skipper, T. N., and Russell, A.
 603 G.: Significant contrasts in aerosol acidity between China and the United States, *Atmos. Chem.*
 604 *Phys.*, 21, 8341–8356, <https://doi.org/10.5194/acp-21-8341-2021>, 2021.

605 Zhang, G., Ding, C., Jiang, X., Pan, G., Wei, X., and Sun, Y.: Chemical compositions and sources
 606 contribution of atmospheric particles at a typical steel industrial urban site, *Sci. Rep.*, 10, 7654,
 607 <https://doi.org/10.1038/s41598-020-64519-x>, 2020.

608 Zhang, Z., Dong, Z., Zhang, C., Qian, G., and Lei, C.: The geochemical characteristics of dust material
 609 and dust sources identification in northwestern China, *J. Geochem. Explor.*, 175, 148–155,
 610 <https://doi.org/10.1016/j.gexplo.2016.11.006>, 2017.

611 Zhang, Z., Kuang, Z., Yu, C., Wu, D., Shi, Q., Zhang, S., Wang, Z., and Liu, D.: Trans–boundary dust
 612 transport of dust storms in Northern China: A study utilizing ground–based lidar network and
 613 CALIPSO satellite, *Remote sens.*, 16, 1196, <https://doi.org/10.3390/rs16071196>, 2024.

614 Zheng, G., Su, H., and Cheng, Y.: Revisiting the key driving processes of the decadal trend of aerosol
 615 acidity in the U.S, *Acs. Environ. Au.*, 2, 346–353, <https://doi.org/10.1021/acsenvironau.1c00055>,
 616 2022.

617 Zheng, G., Su, H., Wang, S., Andreae, M. O., Pöschl, U., and Cheng, Y.: Multiphase buffer theory
 618 explains contrasts in atmospheric aerosol acidity, *Science.*, 369, 1374–1377,
 619 <https://doi.org/10.1126/science.aba3719>, 2020.

620 Zhou, M., Zheng, G., Wang, H., Qiao, L., Zhu, S., Huang, D., An, J., Lou, S., Tao, S., Wang, Q., Yan,
 621 R., Ma, Y., Chen, C., Cheng, Y., Su, H., and Huang, C.: Long-term trends and drivers of aerosol
 622 pH in eastern China, *Atmos. Chem. Phys.*, 22, 13833–13844, [https://doi.org/10.5194/acp-22-](https://doi.org/10.5194/acp-22-13833-2022)
 623 [13833-2022](https://doi.org/10.5194/acp-22-13833-2022), 2022.

624 Zhou, W., Gao, M., He, Y., Wang, Q., Xie, C., Xu, W., Zhao, J., Du, W., Qiu, Y., Lei, L., Fu, P., Wang,

625 Z., Worsnop, D. R., Zhang, Q., and Sun, Y.: Response of aerosol chemistry to clean air action in
626 Beijing, China: Insights from two-year ACSM measurements and model simulations, *Environ*
627 *Pollut.*, 255, 113345, <https://doi.org/10.1016/j.envpol.2019.113345>, 2019.

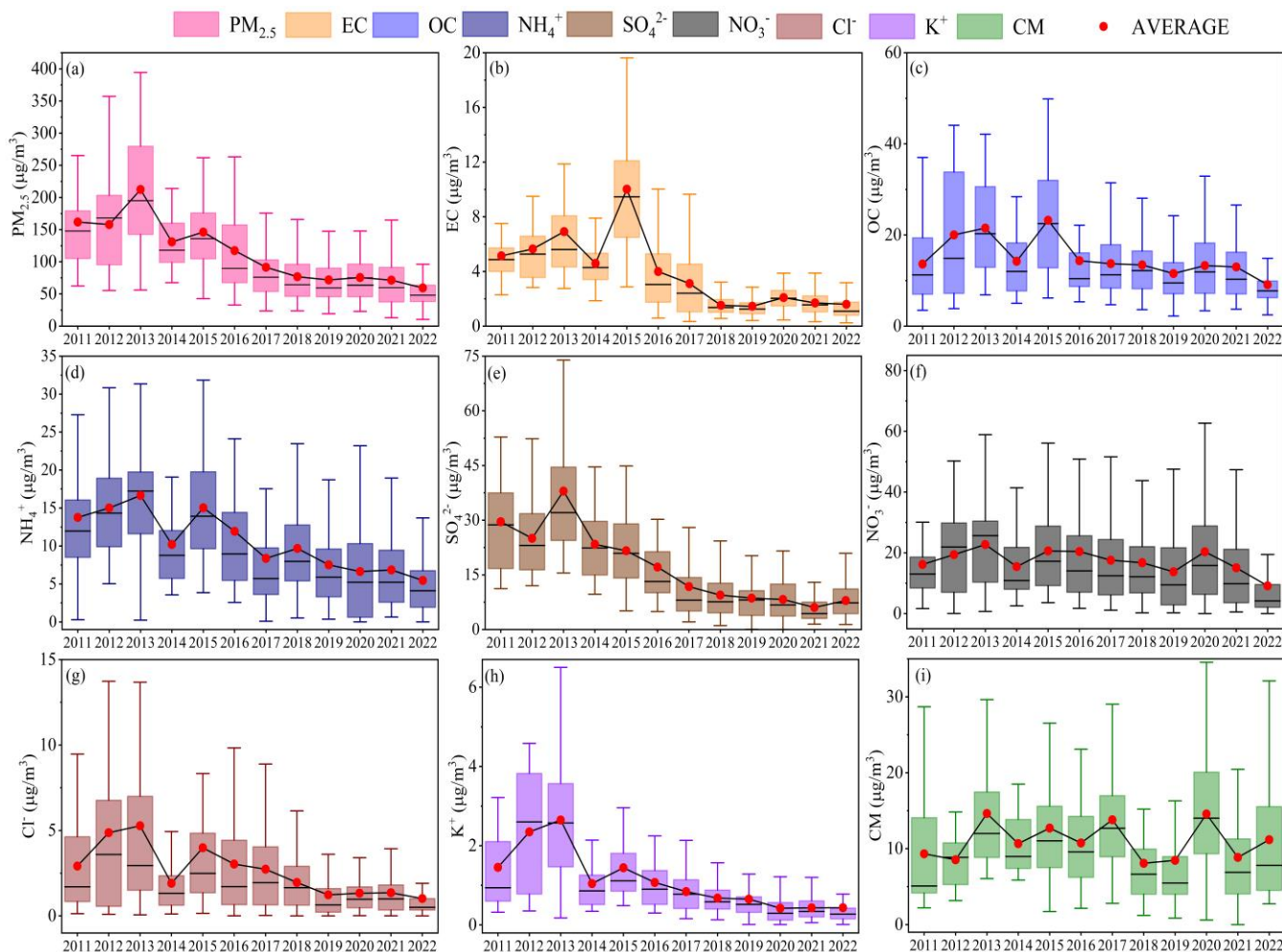
628 Zuend, A. and Seinfeld, J. H.: Modeling the gas-particle partitioning of secondary organic aerosol: the
629 importance of liquid-liquid phase separation, *Atmos. Chem. Phys.*, 12, 3857–3882,
630 <https://doi.org/10.5194/acp-12-3857-2012>, 2012.

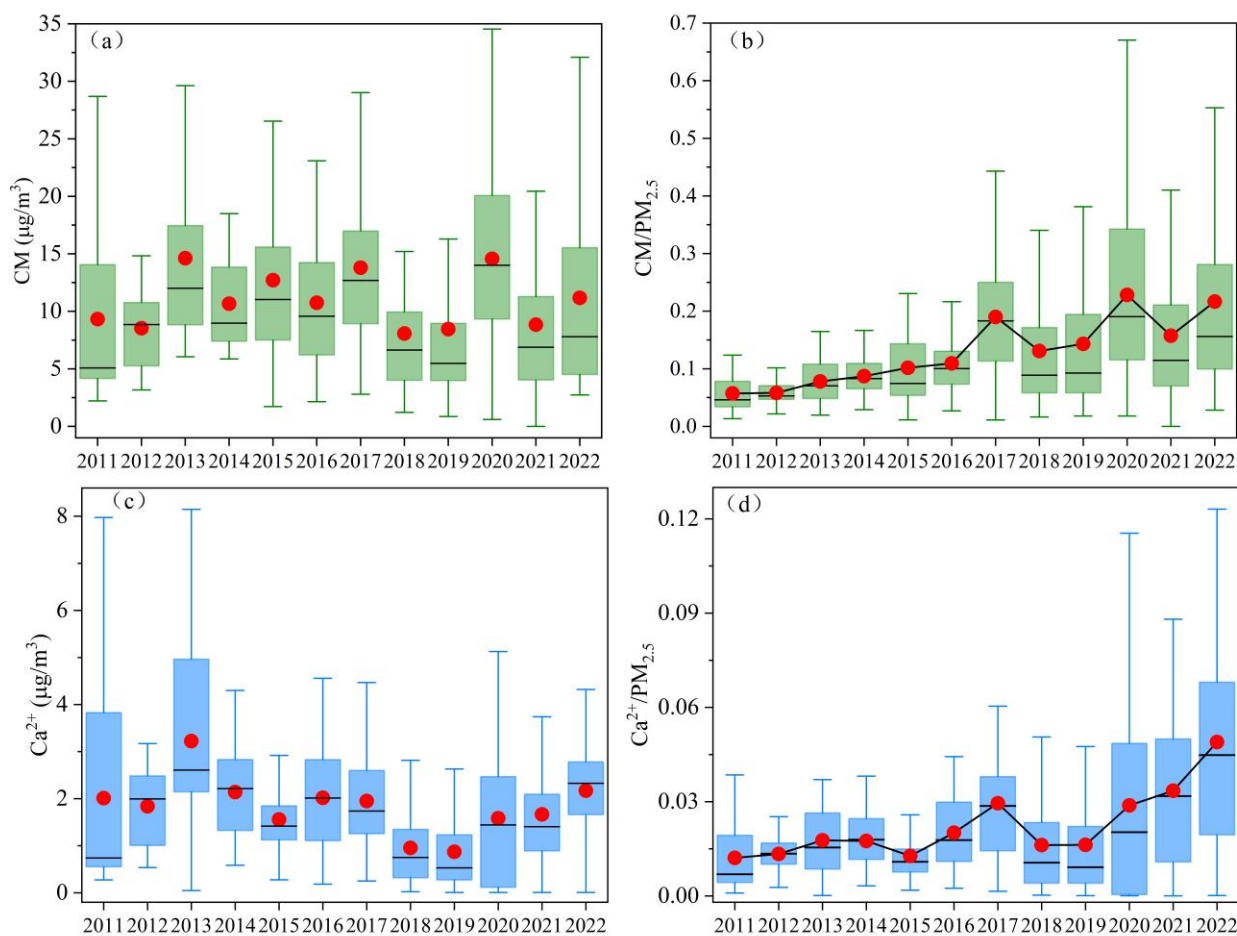
631 Zuend, A., Marcolli, C., Peter, T., and Seinfeld, J. H.: Computation of liquid-liquid equilibria and phase
632 stabilities: implications for RH-dependent gas/particle partitioning of organic-inorganic aerosols,
633 *Atmos. Chem. Phys.*, 10, 7795–7820, <https://doi.org/10.5194/acp-10-7795-2010>, 2010.

634

636

637 Figure 1. Long-term trends in the concentrations of PM_{2.5} and its chemical components in from 2011
638 to 2022 in Zhengzhou. Box plots depict annual averages (red dots) and medians (black lines), the
639 top, middle, and bottom lines represent the 75, 50, and 25 percentiles of statistical data, respectively,
640 and the upper and lower whiskers represent the 90 and 10 percentiles of statistical data, respectively.





641

642 Figure 2. (a) and (c) Long-term trends in CM and Ca²⁺ concentrations in Zhengzhou from 2011 to
 643 2022, respectively. Box plots depict annual averages (red dots) and medians (black lines). (b) and (d)
 644 Long-term trends in the proportions of CM and Ca²⁺ in PM_{2.5}, respectively.

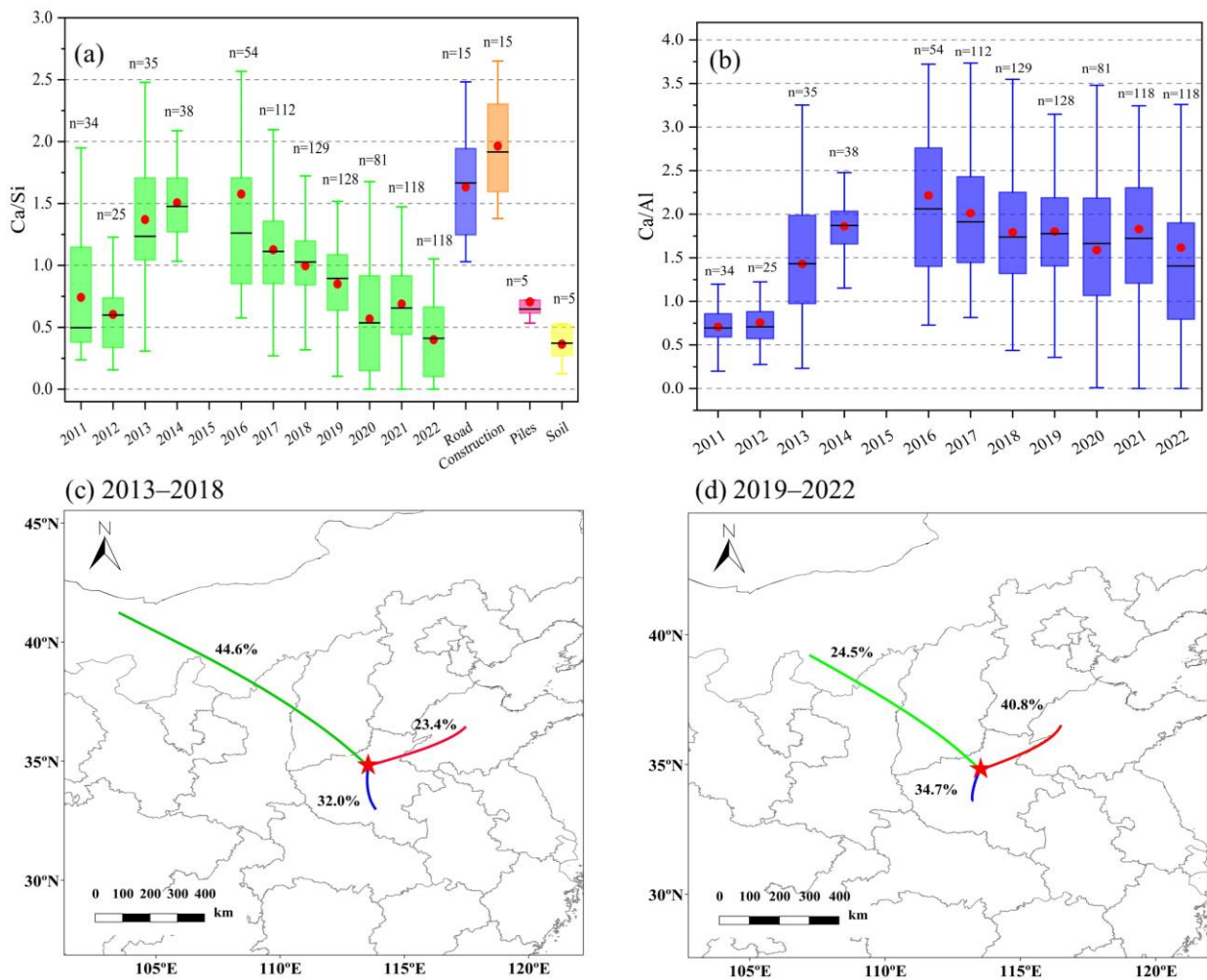


Figure 3. (a) The annual Ca/Si ratios in Zhengzhou from 2011 to 2022 compared with those in various dust sources (specific values and references in Table S5). The red dots and black lines in the box plots represent the annual averages and medians, respectively, with n indicating the sample size. (b) The Ca/Al ratios in Zhengzhou from 2011 to 2022. The red dots and black lines in the box plots represent the annual averages and medians, respectively, with n indicating the sample size. (c) and (d) The transport pathways of CM during 2013–2018 and 2019–2022, respectively.

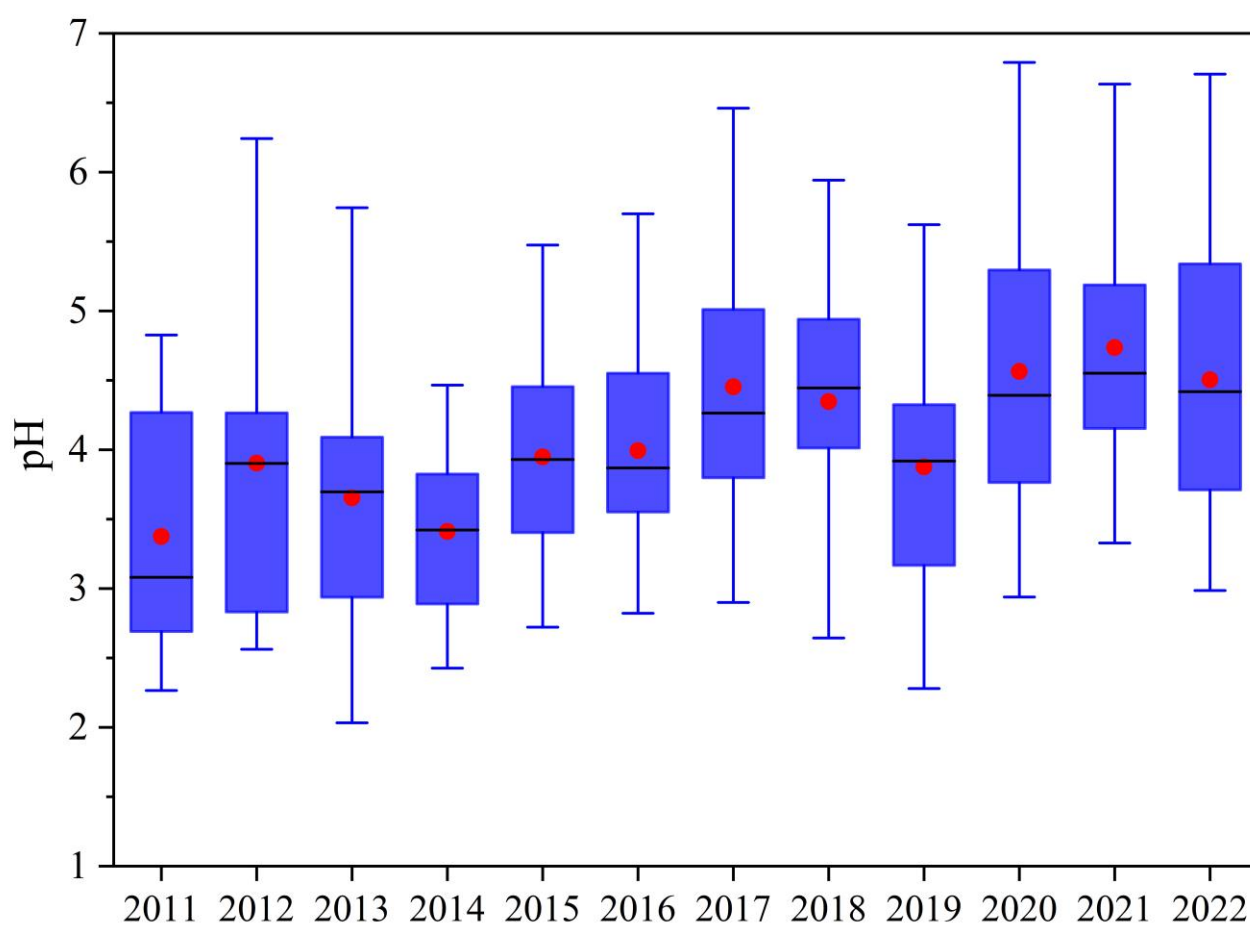


Figure 4. The time series of particle pH in Zhengzhou from 2011 to 2022. In the boxplots, red dots and black lines represent the annual mean and median values, respectively.

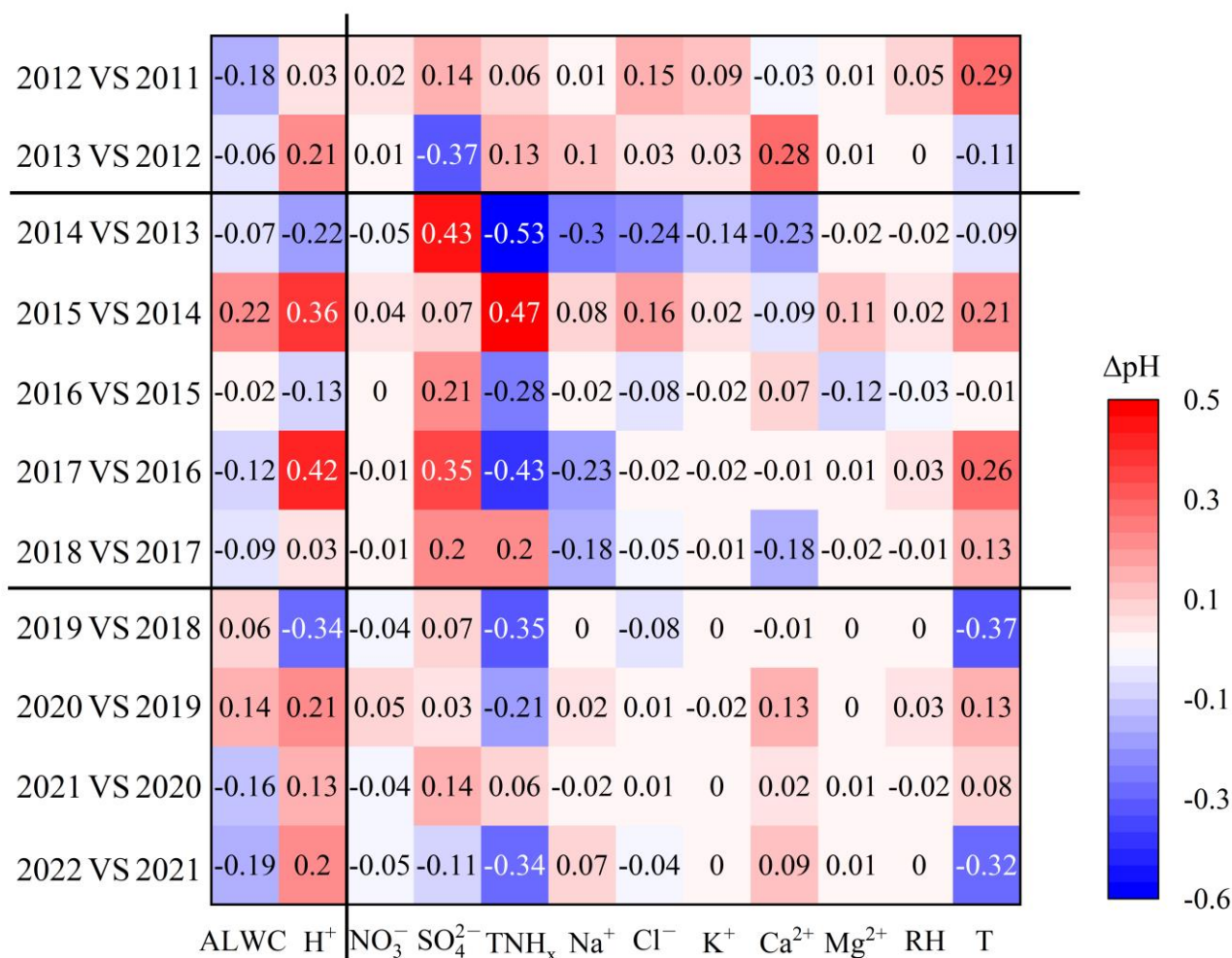


Figure 5. Contribution of each component to the changes in pH (ΔpH) between adjacent years. The difference between component concentrations and meteorological parameters between adjacent years is listed in Table S6.

659 **Table**

660 Table 1. Annual average concentrations of PM_{2.5} and its components from 2011 to 2022 in Zhengzhou,
661 China (µg/m³).

Years	PM _{2.5}	EC	OC	NO ₃ ⁻	SO ₄ ²⁻	NH ₄ ⁺	CM	Ca ²⁺
2011	161.9±81.4	5.1±2.1	13.6±8.6	16.2±11.2	29.6±14.3	13.8±8.3	9.3±7.3	2.0±2.2
2012	157.9±71.2	5.6±2.5	20.0±13.4	20.2±13.7	25.0±11.2	15.0±7.1	8.5±3.4	1.8±0.8
2013	212.4±101.5	6.9±3.8	21.5±10.4	22.7±13.2	38.0±19.9	17.1±6.9	14.6±8.3	3.2±2.1
2014	130.8±48.7	4.6±2.0	14.2±8.2	15.5±10.8	23.4±9.3	10.2±6.2	10.7±4.4	2.1±1.0
2015	146.1±61.0	10.0±4.7	23.2±11.6	20.6±14.5	21.6±9.8	15.7±7.5	12.7±6.8	1.6±0.7
2016	117.4±73.5	4.0±2.8	14.4±10.0	20.4±18.7	17.1±11.3	11.9±10.6	10.8±5.3	2.0±1.1
2017	91.5±61.1	3.1±2.5	13.7±7.5	17.6±15.9	11.8±11.6	8.4±7.9	13.8±6.5	2.0±1.0
2018	76.8±41.6	1.5±0.7	13.4±7.3	16.7±13.5	9.4±6.0	9.7±6.1	8.1±5.7	1.0±0.8
2019	68.4±34.8	1.5±0.8	11.5±6.8	13.8±13.9	8.6±6.4	7.5±6.1	8.5±7.8	0.9±0.9
2020	75.5±31.8	2.1±0.9	13.3±7.9	18.6±14.2	8.3±5.6	6.7±6.6	14.6±7.6	1.6±1.4
2021	71.5±45.9	1.7±0.9	13.0±8.0	15.1±15.1	6.1±4.5	6.8±6.0	8.9±7.0	1.7±1.2
2022	59.5±41.1	1.6±1.5	9.1±8.1	10.0±14.4	7.9±4.5	5.5±5.4	11.2±8.3	2.2±1.1

662

663